# Supporting information for:
# Polythermal conditions in small glaciers in the Swiss Alps

Janosch Beer[1,2], Mylène Jacquemart[1,2], Matthias Huss[1,2,6], Ilaria Santin[1,2], Gabriela Clara Racz[3], Christophe Ogier[1,2], Saskia Gindraux[4], Leo Hösli[1,2], Raphael Moser[1,2], James Irving[3], Mauro Fischer[5,7], and Daniel Farinotti[1,2]

[1]Laboratory of Hydraulics, Hydrology and Glaciology (VAW), ETH Zurich, Zurich, Switzerland
[2]Swiss Federal Institute for Forest, Snow and Landscape Research (WSL), bâtiment ALPOLE, Sion, Switzerland
[3]University of Lausanne, Institute of Earth Sciences, Lausanne, Switzerland
[4]Centre de recherche sur l'environnement alpin (CREALP), Sion, Switzerland
[5]Institute of Geography, University of Bern, Bern, Switzerland
[6]Department of Geosciences, University of Fribourg, Fribourg, Switzerland
[7]Oeschger Centre for Climate Change Research, University of Bern, Bern, Switzerland

**Contents of this file**

This supplement follows the structure of the main paper and provides additional figures and tables supporting the methods, field installations, and results described therein.

# 1 Englacial temperature observations

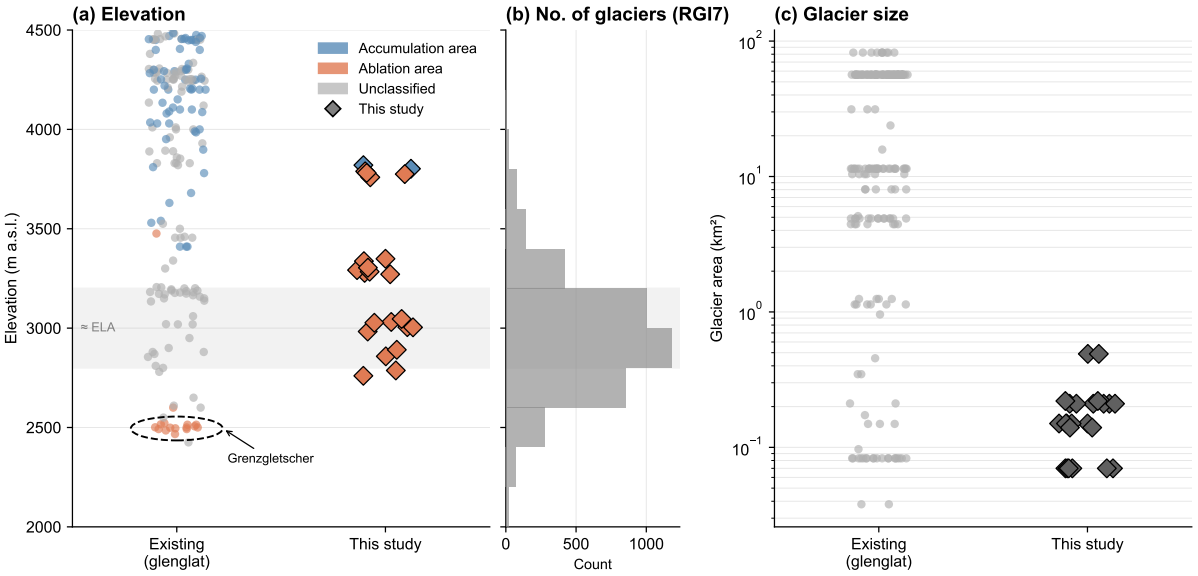


**Figure S1.** Observational bias in Alpine englacial temperature measurements. (a) Borehole elevations in glenglat (Jacquemart and Welty, 2024) and this study, the colour indicates ablation or accumulation area; the dashed ellipse marks Grenzgletscher, which accounts for nearly all measurements declared as ablation-area measurements. (b) RGI7 region 11 glacier elevation distribution (RGI Consortium, 2023). (c) Glacier area of instrumented glaciers.

## 2 Methods and instrumentation

### 2.1 Drilling equipment

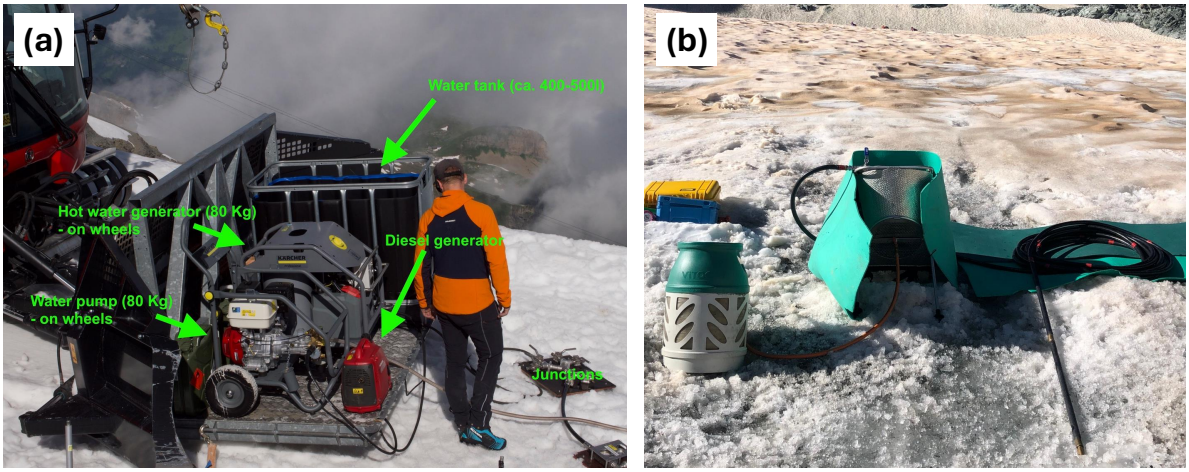


**Figure S2.** Drilling equipment used in this study. (a) Kärcher hot-water drilling unit comprising water tank, diesel heater, pump and hose. The system is capable of delivering water at approximately 80°C through a 2 m rigid metal drill stem. (b) Lightweight portable Heucke steam drill usable as a backpack (Heucke, 1999).

## 2.2 Borehole instrumentation

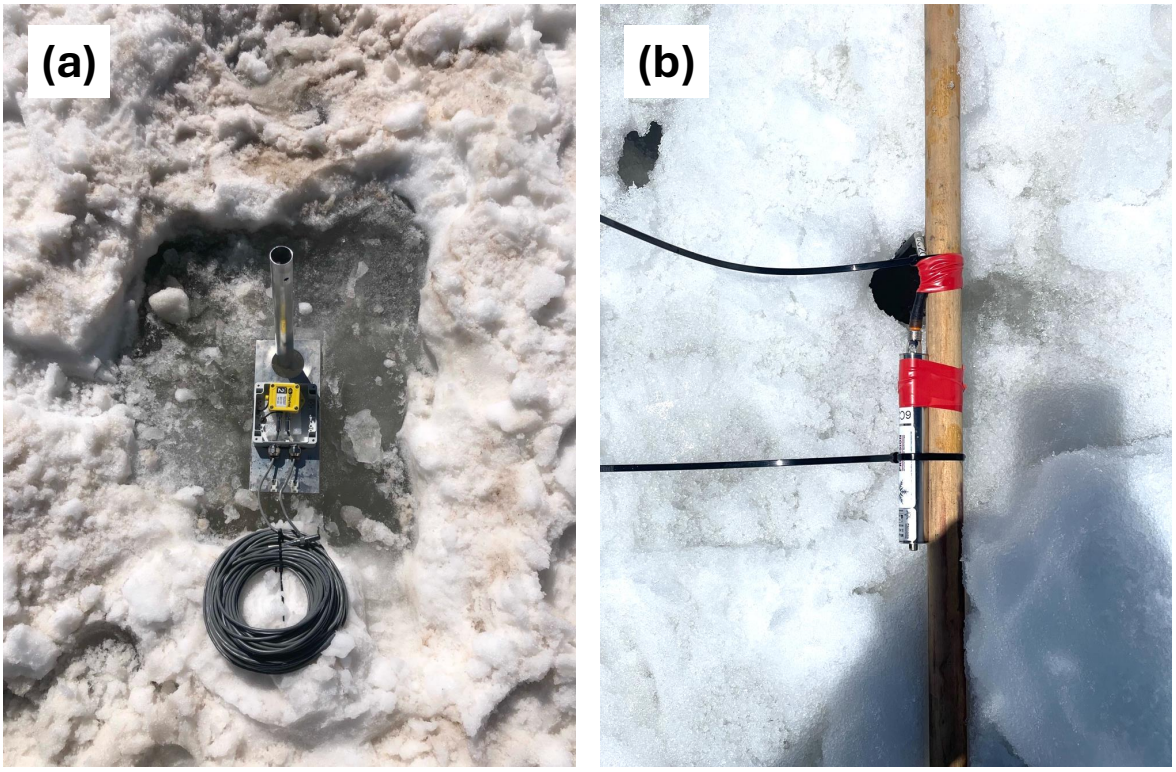


**Figure S3.** Borehole instrumentation used in this study. (a) Shallow boreholes were equipped with a Tinytag Plus 2 (TGP-4520) logger connected to two thermistors, typically placed at 10 and 15 m depth. The logger was housed in a weatherproof logger box mounted on an aluminium plate attached to an ablation stake. (b) Deep boreholes were instrumented with Geoprecision TNode HD thermistor chains containing multiple sensors. The chain logger was fixed to a 1-m wooden stick placed across the borehole top.

### 2.3 Thermistor calibration

All thermistors were calibrated prior to field deployment to correct for sensor-specific offsets relative to 0 °C. Calibration consisted of submerging the sensors in a temperature-controlled bath for approximately two hours to ensure thermal equilibration. To identify stable periods in the recorded signal, rolling statistics were computed from the temperature time series. For a time series $x_1, x_2, \ldots, x_N$, the rolling mean and standard deviation at time $t$ using a window size $w$ are defined as

$$\mu_t = \frac{1}{w} \sum_{i=t-w+1}^{t} x_i, \qquad t \geq w, \tag{1}$$

$$\sigma_t = \sqrt{\frac{1}{w} \sum_{i=t-w+1}^{t} (x_i - \mu_t)^2}, \qquad t \geq w. \tag{2}$$

A period was classified as thermally stable when $\sigma_t < 0.1$ °C, and the rolling mean over this interval ($w = 10$ samples, corresponding to 300 s) was taken as the calibration offset for each sensor.

Tinytag thermistors were calibrated using an ice-bath setup at 0 °C (Fig. S4a). A Geoprecision thermistor (accuracy $\pm 0.05$ °C) submerged simultaneously served as a reference and showed only minor deviations from 0 °C. Geoprecision chains were calibrated in a temperature-controlled alcohol bath (Huber CC245 WL), with an ISOTECH F250 high-precision thermometer (accuracy $\pm 0.01$ °C) as an external reference, providing the most precise calibration applied in this study.

The median offset is 0.302 °C for the Tinytag sensors and $-0.004$ °C for the Geoprecision sensors (Fig. S5). One extreme offset of 5.95 °C was identified for the Tinytag logger eventually deployed at borehole GT2TT on Glacier de Tortin. After consultation with the manufacturer, this anomaly was attributed to water infiltration into the logger housing. This sensor was consequently excluded from further analysis, and no englacial temperature data are available for GT2TT. The remaining Tinytag offsets range from 0.19 to 1.17 °C, while the Geoprecision offsets fall within a much narrower range of $-0.182$ to $0.121$ °C.

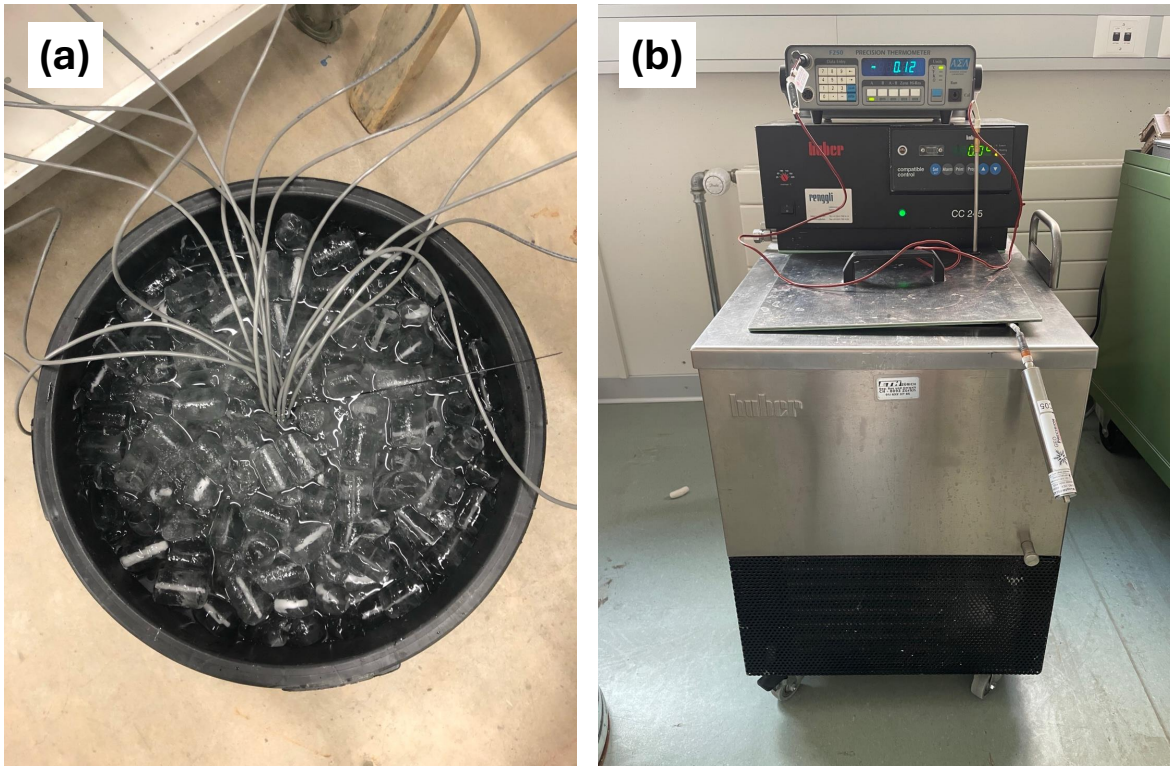


**Figure S4.** Temperature-controlled baths used for calibrating thermistor sensors prior to field deployment. (a) Ice bath used to determine 0 °C offsets for Tinytag thermistors. (b) Alcohol bath (Huber CC245 WL) and high-precision thermometer (ISOTECH F250) used to determine 0 °C offsets for Geoprecision thermistors.

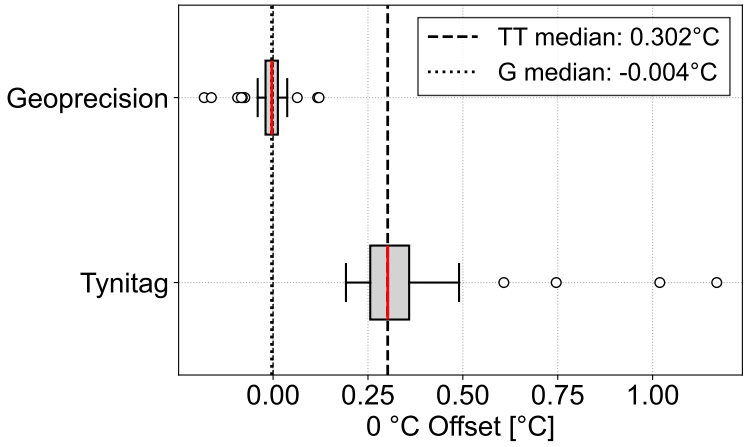


**Figure S5.** Distribution of calculated 0 °C offsets for the Geoprecision (dotted) and Tinytag (dashed) thermistors.

### 2.4 Englacial temperature interpolation

Borehole temperature data were interpolated to a continuous two-dimensional field along glacier profiles using Radial Basis Function (RBF) interpolation (Hardy, 1971), implemented via the `RBFInterpolator` routine of the SciPy library (Virtanen et al., 2020). The RBF uses a multiquadric kernel ($\phi(r) = \sqrt{r^2 + \epsilon^2}$), where $r$ is the Euclidean distance between two points in the scaled coordinate space and $\epsilon$ is a shape parameter controlling the width of the basis functions, set to its default value of 1.

For each borehole $j$, the vertical elevation of thermistor probe $k$ is

$$z_{j,k} = z_{s,j} - d_{j,k}, \tag{3}$$

where $d_{j,k}$ is the sensor depth and $z_{s,j}$ is the surface elevation at the borehole. Temperature at arbitrary points $(x, z)$ is estimated as

$$T(x,z) = \sum_{m=1}^{M} \lambda_m \phi(\|\mathbf{p}_m - (x, wz)\|), \tag{4}$$

where $M$ is the total number of measurement points, $\lambda_m$ are weights determined by fitting the RBF to the observations, and $\mathbf{p}_m = (x_m, wz_m)$ are the coordinate-scaled positions of each measurement. Distances are computed as

$$\|\mathbf{p}_m - (x, wz)\| = \sqrt{(x_m - x)^2 + (wz_m - wz)^2}. \tag{5}$$

The vertical coordinate is scaled by a factor $w > 1$ to reflect the stronger vertical than horizontal temperature gradients characteristic of glacier ice (Cuffey and Paterson, 2010). The scaling factor was empirically set to $w = 2.5$. The interpolated field was evaluated on a regular grid spanning the glacier cross-section and masked to the glacier geometry.

### 2.5 Cold-temperate transition surface detection

The position of the cold-temperate transition surface (CTS) was identified as the boundary between grid cells where the interpolated temperature reached the local pressure melting point and those where it remained below. The melting point depression follows the Clausius-Clapeyron relation:

$$T_m(d) = -\beta \cdot d, \tag{6}$$

where $T_m$ is the melting point (°C), $d$ is the depth below the surface (m), and $\beta = 8.7 \times 10^{-4}$ °C m$^{-1}$ is the pressure-melting coefficient for air-saturated ice (Cuffey and Paterson, 2010). The depth at elevation $z$ and horizontal position $x$ is:

$$h(x,z) = z_s(x) - z, \tag{7}$$

where $z_s(x)$ is the surface elevation at horizontal location $x$. Grid cells were flagged as temperate where the interpolated temperature satisfied:

$$|T(x,z) - T_m(h)| \leq \delta_{\text{CTS}}, \tag{8}$$

where $\delta_{\text{CTS}} = 0.05$ °C.

### 2.6 Depth of zero annual amplitude

The depth of zero annual amplitude (ZAA) marks the depth below which seasonal temperature fluctuations become negligible (here defined as variations $< 0.05$ °C). To estimate the ZAA from the Tinytag borehole records, we computed the seasonal amplitude at each sensor as the 2nd–98th percentile range of the measured time series, excluding short-lived transient signals such as refreezing meltwater events. We then fitted an exponential decay function

$$A(z) = A_0 \exp\left(-\frac{z}{d}\right) \tag{9}$$

to the amplitude-depth pairs using least-squares regression, where $A_0$ is the surface amplitude and $d$ is the characteristic decay depth, both determined from the fit. The ZAA was then defined as the depth at which the fitted amplitude falls below 0.05 °C. For glaciers where the deepest sensor exhibited amplitudes exceeding the 0.3 °C threshold, the ZAA could not be reliably constrained from the available data and is not reported.

### 2.7 Ground-penetrating radar and ice thickness

Two pulse-based GPR systems were used in this study (Fig. S6): a ground-based system deployed at all sites (100 MHz for all glaciers except Alphubel where we used a 250 MHz center frequency), and an uncrewed aerial vehicle (UAV)-based system (80 MHz center frequency) used at Hohsaasgletscher (Ruols et al., 2023). Each system required a dedicated processing workflow, described in the following sections.

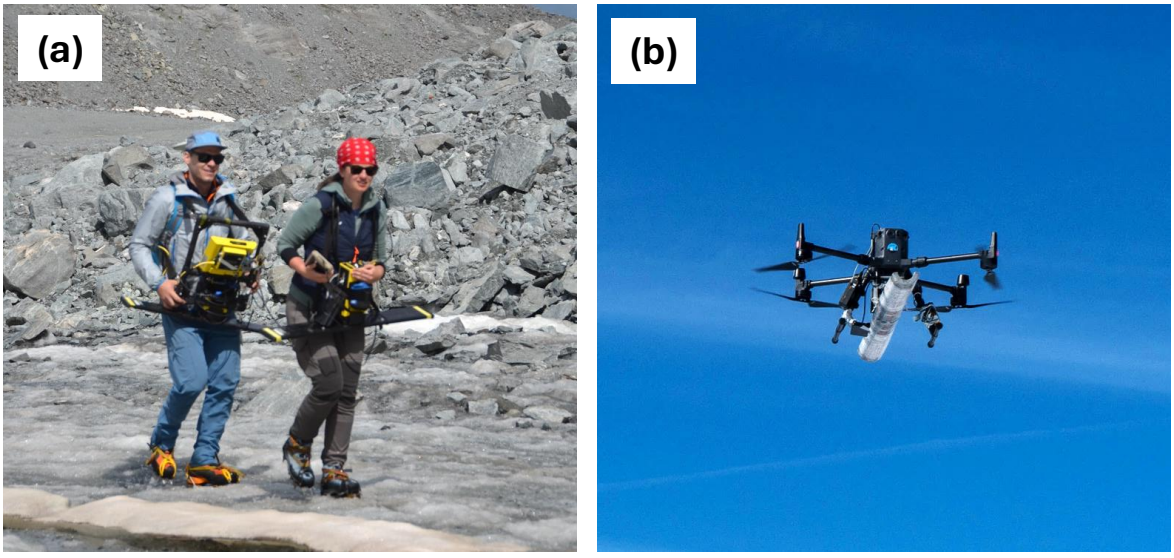


**Figure S6.** GPR systems used in this study. (a) Ground-based system, carried either on foot or on a sledge. (b) UAV-based system as developed by Ruols et al. (2023).

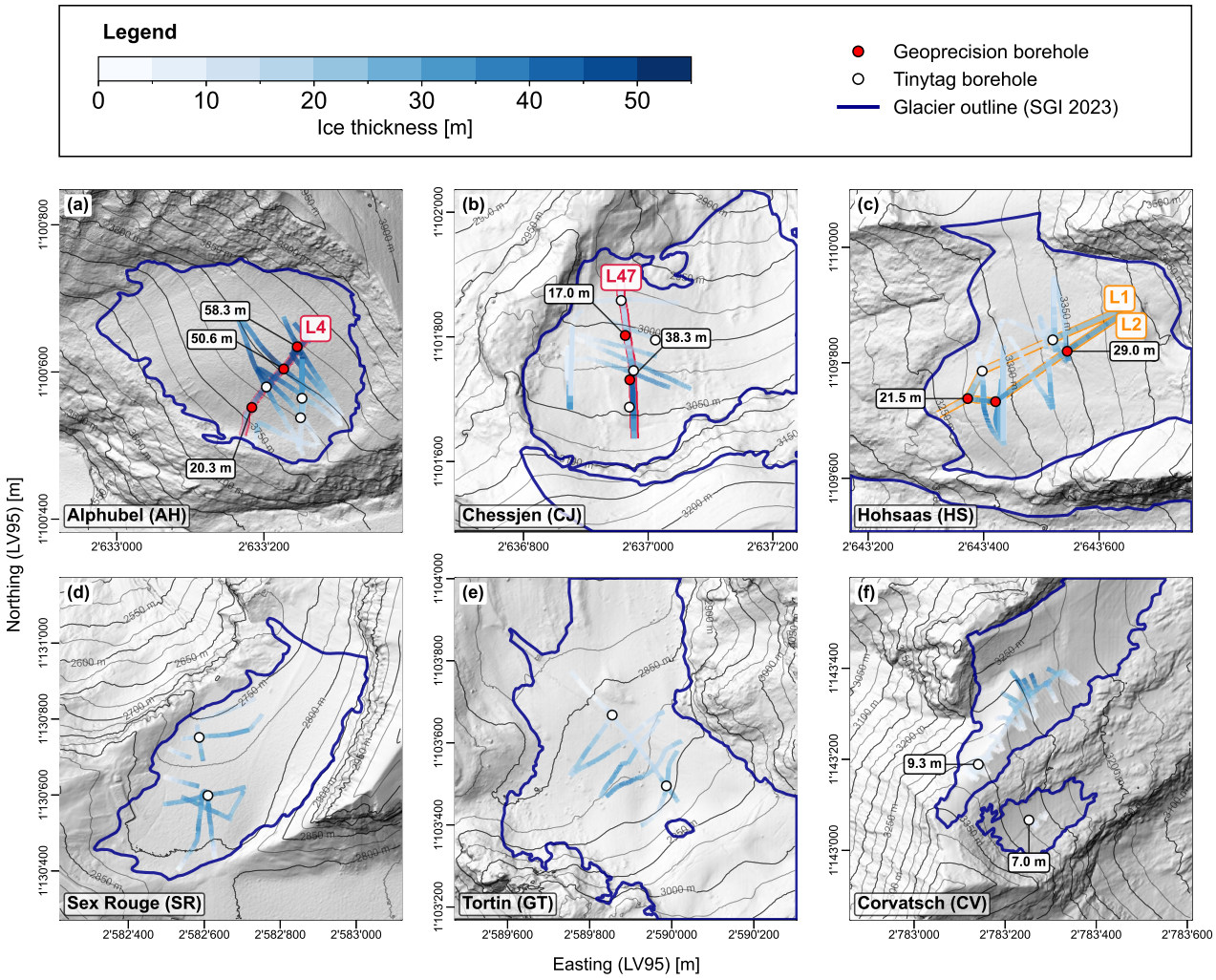


**Figure S7.** GPR survey profiles coloured by measured ice thickness, draped over a shaded-relief DEM (Swisstopo, 2023) for (a) Alphubel, (b) Chessjen, (c) Hohsaas (L1 and L2 derived from UAV-based GPR), (d) Sex Rouge, (e) Tortin, and (f) Corvatsch. Profiles used for subsequent ice-temperature interpolation are marked in red/orange. Borehole locations are distinguished by manufacturer (Geoprecision, Tinytag). Boreholes that reached the glacier bed are annotated with the measured drilling depth.

### 2.7.1 Ground-based GPR processing

A standard processing flow was applied to all ground-based GPR data using the cloud-based Geolitix software (Geolitix Technologies Inc., 2020):

1. time zero correction based on the direct wave arrival,
2. background noise removal , performed by average trace subtraction over a trace window of the entire recorded time window,
3. Butterworth band-pass filtering (50–200 MHz),
4. trace binning at 0.02 m spatial sampling,
5. surface reflection picking and elevation referencing, where the picked first arrival was used to tie each trace to the antenna elevation measured by the differential GNSS at the corresponding position,
6. manual time-varying gain function, with an approximately exponential increase with two-way travel times, and
7. imaging and time-to-depth conversion by Kirchhoff migration, assuming a constant radar wave speed in ice of 0.168 m/ns.

### 2.7.2 UAV-based GPR processing

The UAV-based GPR data from Hohsaas were processed using a customized workflow, adapted from Ruols et al. (2023), to produce a 3D data cube imaged in depth. The workflow involved the following steps:

1. Synchronization and positioning: GPR traces (acquired at 14 Hz) were synchronized with high-precision RTK GNSS data (acquired at 5 Hz) using common GPS time. Individual trace coordinates were corrected for the static offset between the GNSS and GPR antennas, and were adjusted for the drone pitch, roll, and yaw to determine the precise measurement locations of the GPR antenna center.
2. Signal processing and binning: Basic signal processing included (i) a time-zero correction to align the first arrival with the transmitter fire time, (ii) early signal muting to suppress high-amplitude energy associated with the direct pulse, (iii) mean trace removal using a 30-trace sliding window to eliminate system ringing, and (iv) de-wow filtering to remove low-frequency transients using a 15-point residual median filter in time. The data were then binned onto a regular grid having an along-line spacing of 0.4 m and an across-line spacing of 4 m.
3. Alignment: To correct for small differences in UAV height between adjacent GPR profiles and conform the data to a smooth acquisition surface, static corrections were applied to each trace using a Fourier phase shift. To correct for the effects of internal timing delays specific to the UAV-based GPR system, a cross-correlation-based shift was used to align adjacent odd- and even-numbered flight lines.

4. 3D Migration: Prior to migration, the data were densified to a 2 m across-line spacing using 3D linear interpolation to reduce directional sampling bias. Imagine and time-to-depth conversion was performed using 3D topographic Kirchhoff migration (**?**). A two-layer velocity model was assumed, consisting of an upper air layer ($v = 0.3$ m/ns) and a lower glacier ice layer ($v = 0.168$ m/ns).

5. Modeling glacier geometry: We reconstructed the 3D glacier geometry to provide the geometric framework required for thermal interpolation. First, the basal bedrock reflections were manually picked along 91 binned along-line profiles. These picks were then interpolated into a continuous 3D bedrock surface using locally weighted scatterplot smoothing called lowess (**?**)) with span = 0.02. The glacier surface model was generated by subtracting measurements from the 24-GHz nanoradar altimeter from the smoothed acquisition surface and applying a similar lowess smoothing.

6. Virtual profile extraction: Finally, two virtual down-slope centerlines (L1 and L2), each intersecting three boreholes, were extracted by sampling the 3D GPR data cube and the bed/surface models using a nearest-neighbour approach to retrieve the closest available values.

## 3 Mass balance and firn cover evolution

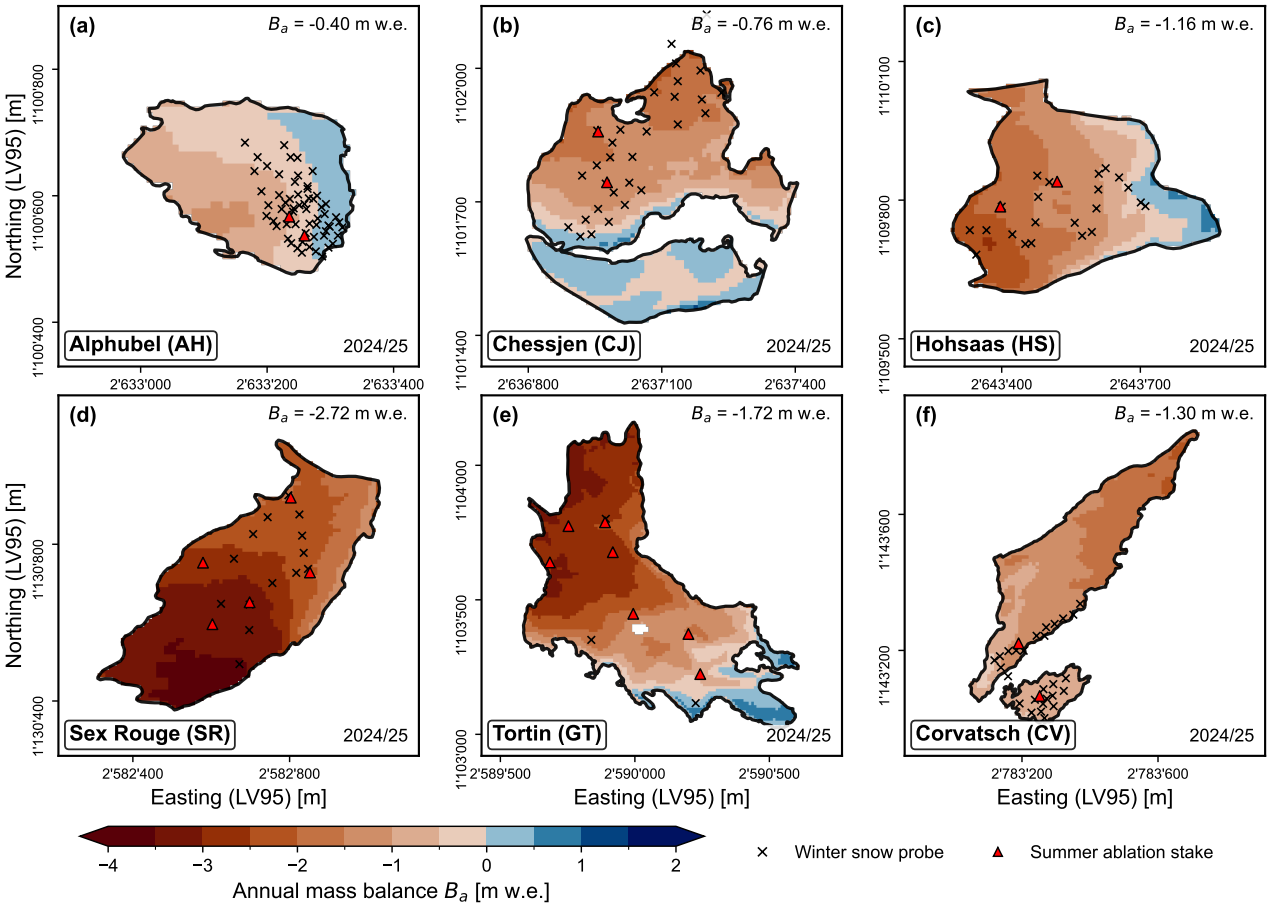


**Figure S8.** Spatially distributed annual mass balance for the 2024/25 hydrological year at all six study sites, derived from the mass balance model of Huss et al. (2021). Black crosses mark snow depth measurement locations from the April/May 2025 field survey, used to constrain the spatial interpolation of winter accumulation. Red triangles mark locations of summer ablation stake readings. Glacier-wide annual mass balance values ($B_a$) are annotated in each panel.

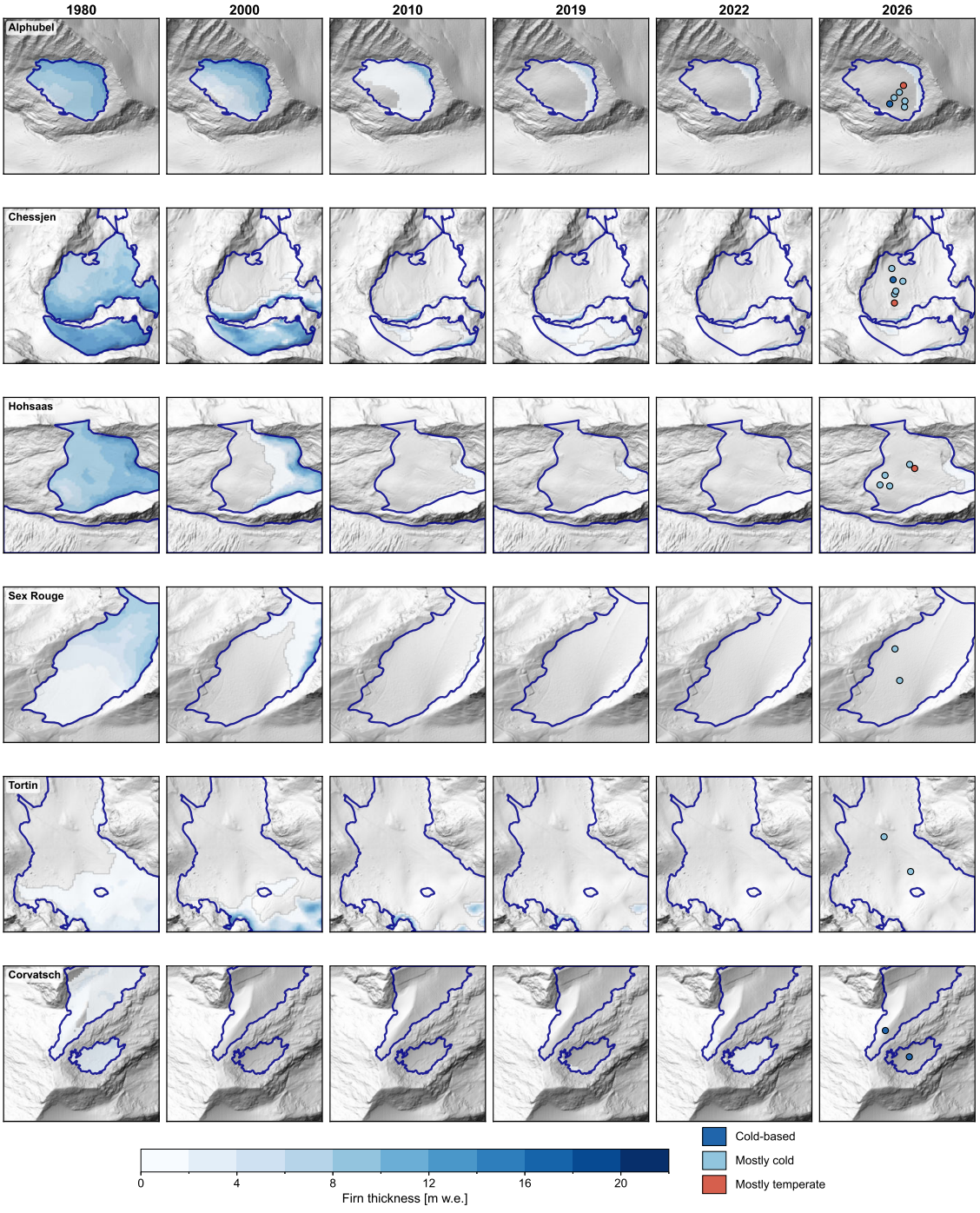


**Figure S9.** Modelled firn thickness (m w.e.) at the six study sites for selected years between 1980 and 2026. Glacier outlines follow the SGI2023. Borehole locations are indicated in the 2026 panel only and coloured by thermal regime (see Sect. 3.3.1 of the main text for category definitions).

(a)

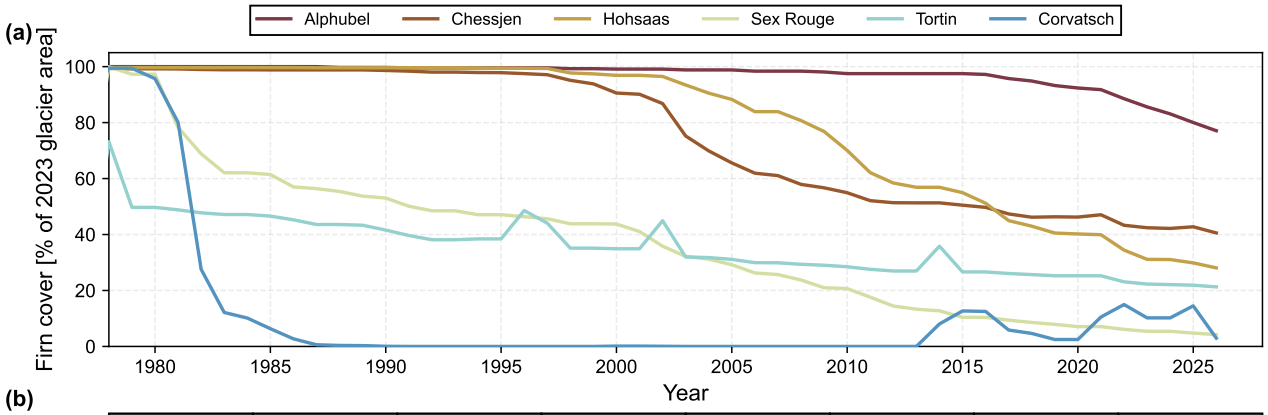


(b)

| | Area [km²] | Firn 1980 [km² / %] | Firn 2026 [km² / %] | Change 1980→2026 [%] | Peak firn [km² / yr] | Mean thick. 2026 [m w.e.] | Mean firn age [yr] | Mean yrs since firn loss |
|---|---|---|---|---|---|---|---|---|
| **Alphubel** | 0.07 | 0.068 / 100 | 0.052 / 77 | -23 | 0.068 / 1975 | 15.2 | 11.8 | 5.7 |
| **Chessjen** | 0.20 | 0.203 / 99 | 0.083 / 41 | -59 | 0.203 / 1978 | 20.0 | 6.8 | 18.4 |
| **Hohsaas** | 0.15 | 0.150 / 100 | 0.042 / 28 | -72 | 0.150 / 1976 | 15.2 | 2.2 | 13.4 |
| **Sex Rouge** | 0.22 | 0.215 / 97 | 0.009 / 4 | -96 | 0.221 / 1978 | 6.6 | — | 31.3 |
| **Tortin** | 0.49 | 0.245 / 50 | 0.105 / 21 | -57 | 0.361 / 1978 | 25.8 | 3.5 | 30.6 |
| **Corvatsch** | 0.17 | 0.158 / 96 | 0.005 / 3 | -97 | 0.165 / 1978 | 1.2 | — | 36.4 |

**Figure S10.** Firn cover evolution and summary statistics for all six study sites, derived from historical mass balance reconstruction. (a) Annual firn cover expressed as a percentage of the 2023 total glacier area from 1975 to 2026. (b) Key firn metrics per glacier: total glacier area, firn extent in 1980 and 2026 ($km^2$ and % of 2023 glacier area), relative change 1980–2026, peak firn extent with corresponding year, mean firn thickness in 2026, and mean years since firn loss for currently firn-free areas.

## 4 Deep borehole temperature time series

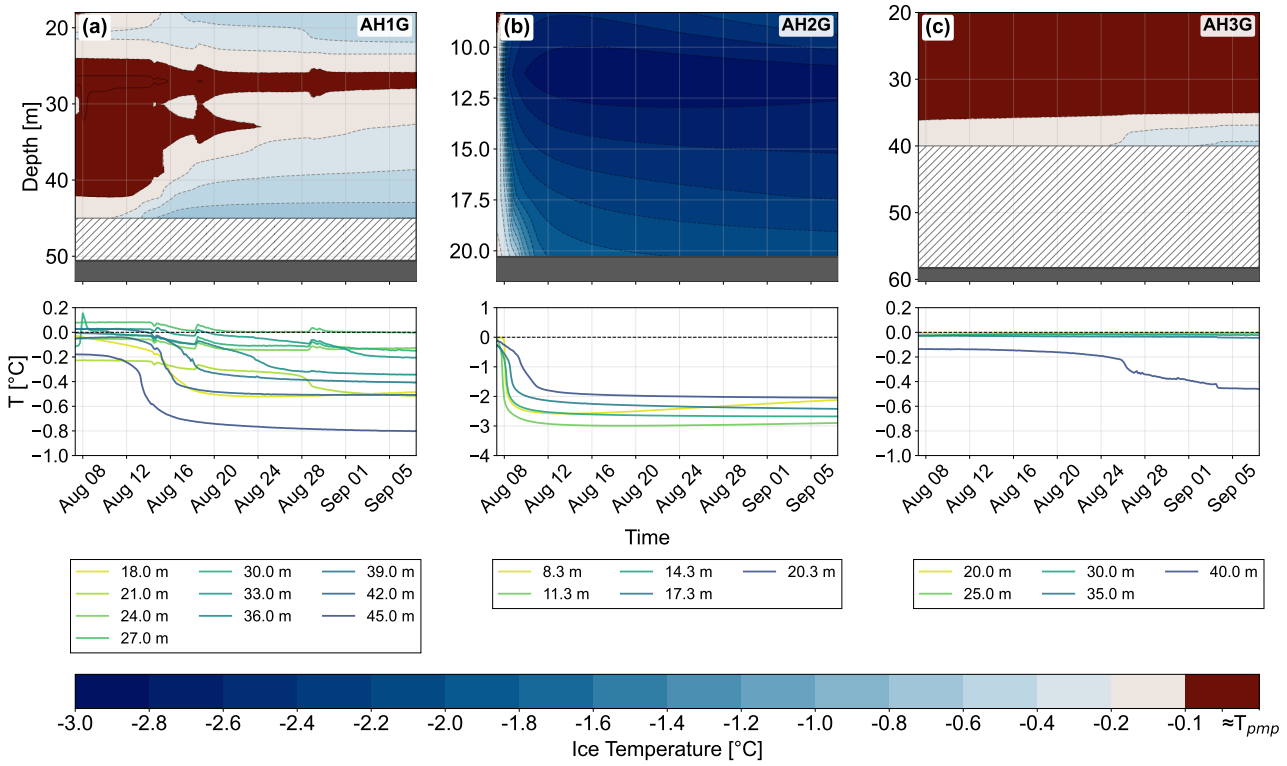


**Figure S11.** Ice-temperature evolution at the three deep thermistor chains on Alphubel South (August–September 2025) for boreholes (a) AH1G, (b) AH2G, and (c) AH3G. Top panels show interpolated ice temperature as a function of time and depth, obtained by one-dimensional interpolation between thermistors; depth increases downward. Dashed contours denote isotherms, including the pressure-dependent melting point $T_{\mathrm{pmp}}$; temperatures at or above $T_{\mathrm{pmp}}$ are classified as temperate and shown in red. Hatched areas indicate depths below the deepest thermistor without measurements, and the dark-gray band marks the measured bedrock depth. Bottom panels show the measured temperature time series at each sensor depth, with 0 °C indicated by a dashed line. The shared colorbar indicates temperature in °C.

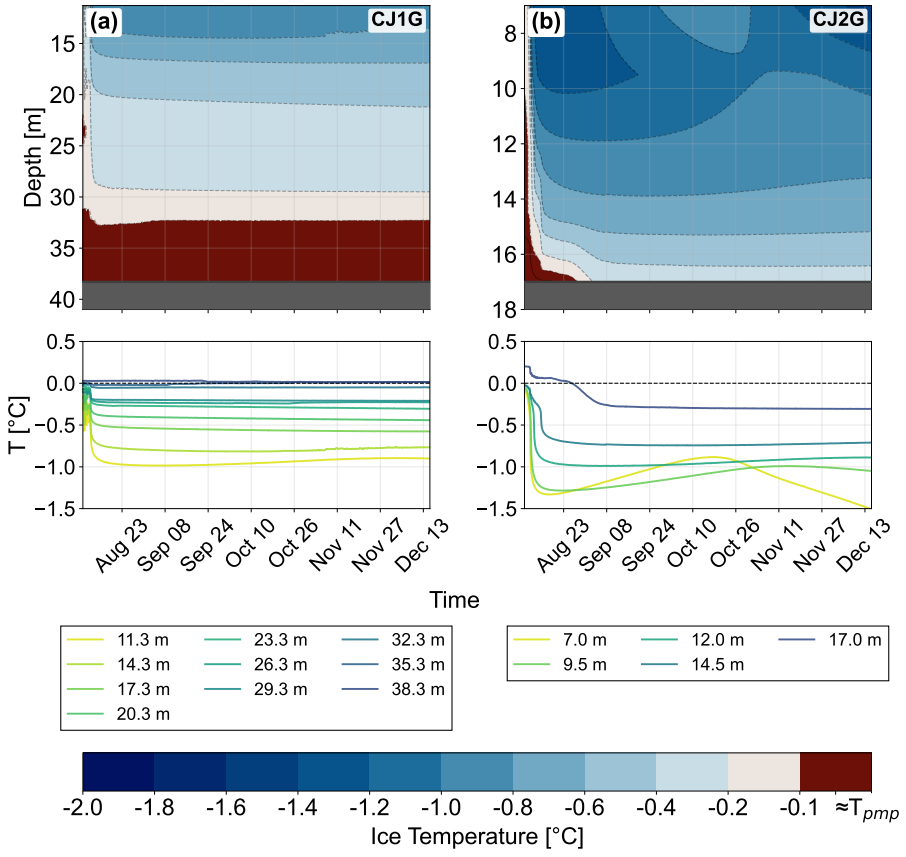


**Figure S12.** Same as Fig. S11 but for Chessjengletscher, boreholes (a) CJ1G and (b) CJ2G.

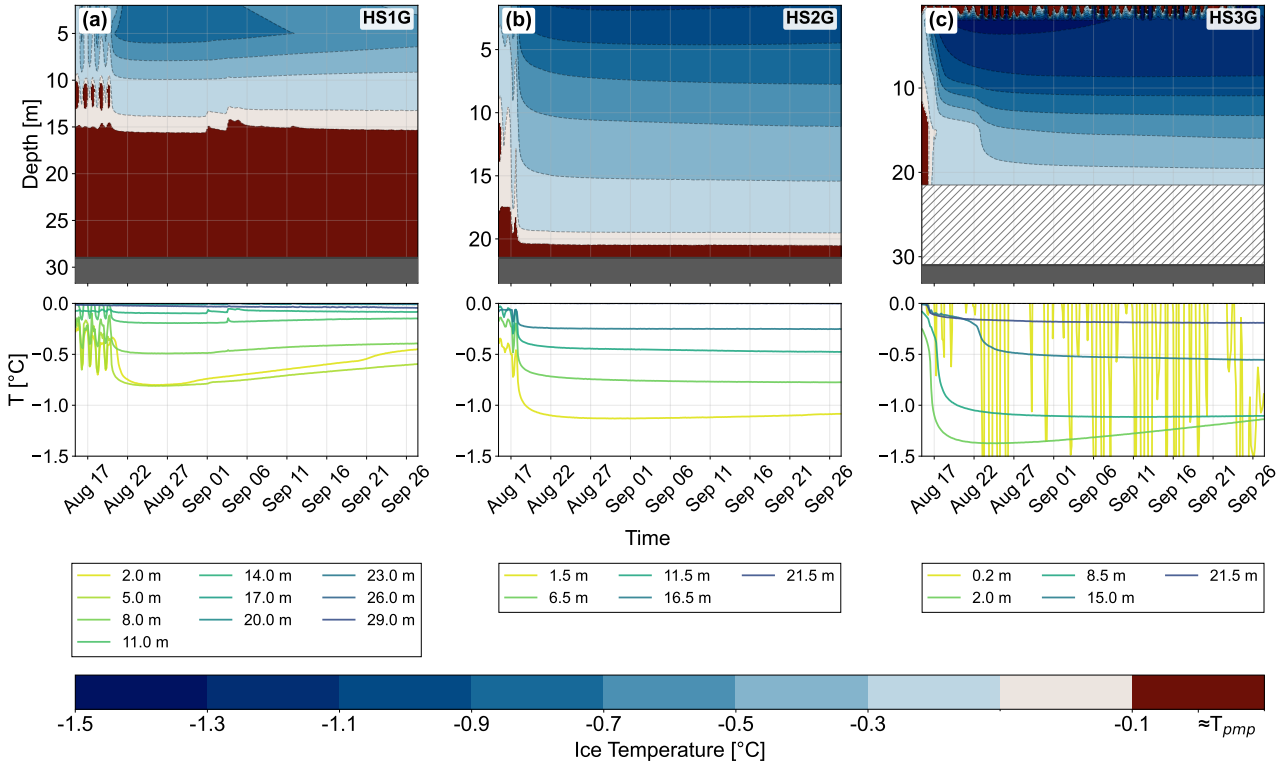


**Figure S13.** Same as Fig. S11 but for Hohsaasgletscher, boreholes (a) HS1G, (b) HS2G, and (c) HS3G.

## 5 Displacement rates

Displacement rates were derived from repeated GNSS measurements at ablation stake locations, conducted between July and September in both 2024 and 2025. For some stakes, reliable displacement rates could not be derived due to stake loss or insufficient measurement intervals, and are therefore not reported.

**Table S14.** Surface displacement rates derived from GNSS measurements for the 2024/2025 hydrological year. Missing values indicate boreholes for which no reliable displacement rate could be derived.

| **Glacier** | **Borehole** | **Displacement rate [m $a^{-1}$]** |
|---|---|---|
| Alphubel South | AH1TT | – |
| | AH2TT | 3.34 |
| Chessjengletscher | CJ1TT | 0.28 |
| | CJ2TT | 1.43 |
| Hohsaasgletscher | HL5TT | – |
| | HL6TT | 3.36 |
| Glacier du Sex Rouge | SR1TT | 5.27 |
| | SR2TT | 5.53 |
| Glacier de Tortin | GT1TT | 1.73 |
| | GT2TT | 1.96 |
| Vadret dal Corvatsch | CV1TT | – |
| | CV2TT | – |

## 6 Historical images Alphubel, Chessjen, Hohsaas

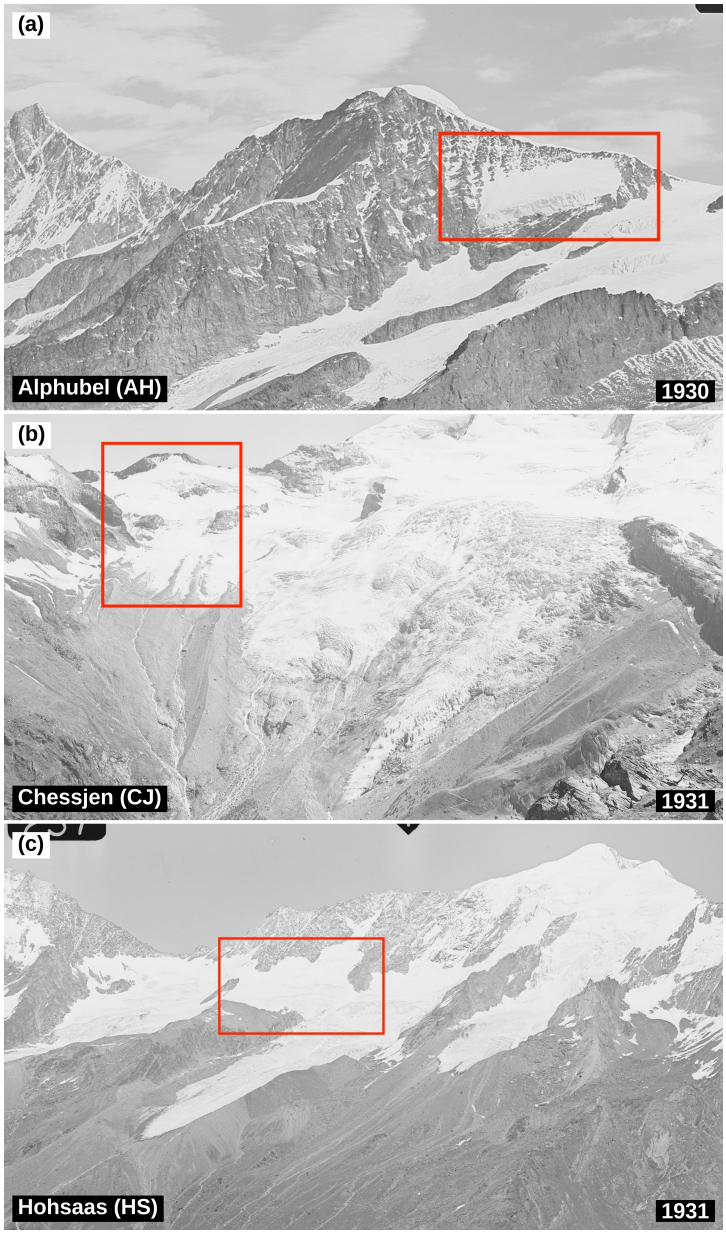


**Figure S15.** Historical photographs of (a) Alphubel on 1930-08-19, (b) Chessjen on 1931-07-16, and (c) Hohsaas on 1931-07-11, illustrating their substantially larger historical extents. Alphubel is expressed as a steep hanging glacier with a prominent calving front, in clear contrast to the valley-type glaciers of Chessjen and Hohsaas, which drain into Feegletscher and Triftgletscher, respectively.Red rectangles indicate the approximate glacier location. Photographs from the swisstopo terrestrial photography archive (Federal Office of Topography swisstopo, 1930–1931).

## References


Cuffey, K. M. and Paterson, W. S. B.: The Physics of Glaciers, Academic Press, ISBN 978-0-08-091912-6, 2010.

Federal Office of Topography swisstopo: Terrestrische Aufnahmen (Lubis), 1930–1931.

Geolitix Technologies Inc.: Geolitix: Cloud-hosted Platform for GPR Data Visualization and Interpretation, 2020.

Hardy, R. L.: Multiquadric Equations of Topography and Other Irregular Surfaces, https://doi.org/10.1029/JB076i008p01905, 1971.

Heucke, E.: A Light Portable Steam-Driven Ice Drill Suitable for Drilling Holes in Ice and Firn, Geografiska Annaler. Series A, Physical Geography, 81, 603–609, 1999.

Huss, M., Bauder, A., Linsbauer, A., Gabbi, J., Kappenberger, G., Steinegger, U., and Farinotti, D.: More than a Century of Direct Glacier Mass-Balance Observations on Claridenfirn, Switzerland, Journal of Glaciology, 67, 697–713, https://doi.org/10.1017/jog.2021.22, 2021.

Jacquemart, M. and Welty, E.: Glenglat: A Database of Global Englacial Temperatures, Earth System Science Data Discussions, pp. 1–47, https://doi.org/10.5194/essd-2024-249, 2024.

RGI Consortium: Randolph Glacier Inventory - A Dataset of Global Glacier Outlines, Version 7, https://doi.org/10.5067/F6JMOVY5NAVZ, 2023.

Ruols, B., Baron, L., and Irving, J.: Development of a Drone-Based Ground-Penetrating Radar System for Efficient and Safe 3D and 4D Surveying of Alpine Glaciers, Journal of Glaciology, 69, 2087–2098, https://doi.org/10.1017/jog.2023.83, 2023.

Swisstopo: SWISSALTI3D – The Digital Elevation Model of Switzerland, https://www.swisstopo.admin.ch, 2023.

Virtanen, P., Gommers, R., Oliphant, T. E., Haberland, M., Reddy, T., Cournapeau, D., Burovski, E., Peterson, P., Weckesser, W., Bright, J., van der Walt, S. J., Brett, M., Wilson, J., Millman, K. J., Mayorov, N., Nelson, A. R. J., Jones, E., Kern, R., Larson, E., Carey, C. J., Polat, İ., Feng, Y., Moore, E. W., VanderPlas, J., Laxalde, D., Perktold, J., Cimrman, R., Henriksen, I., Quintero, E. A., Harris, C. R., Archibald, A. M., Ribeiro, A. H., Pedregosa, F., and van Mulbregt, P.: SciPy 1.0: Fundamental Algorithms for Scientific Computing in Python, Nature Methods, 17, 261–272, https://doi.org/10.1038/s41592-019-0686-2, 2020.